# Modelling turbulent and dispersion heat fluxes in turbulent porous medium flows using the resolved LES data

# Modelling turbulent and dispersion heat fluxes in turbulent porous medium flows using the resolved LES data

Kazuhiko Suga*, Ryu Chikasue, Yusuke Kuwata

*Department of Mechanical Engineering, Osaka Prefecture University, Sakai, Osaka 599-8531, Japan*

**Abstract**

Resolved large eddy simulations (LESs) of turbulent conjugate heat transfer in porous media are performed by the lattice Boltzmann method (LBM) for modelling turbulent and dispersion heat flux terms of the double-averaged energy equation. The considered porous structures are square rod arrays, staggered cube arrays and body centred cubic foam. In the LBM, the double-distribution function method which solves the distribution functions for the velocity and the internal energy is used. For the velocity and thermal fields, the D3Q27 multiple-relaxation-time method and the regularized D3Q19 single-relaxation-time method are applied, respectively. A priori tests using the LES data suggest that the trends of the sum of the dispersion and volume-averaged turbulent heat fluxes can be well captured by the second order gradient diffusion model.

*Keywords:* LES, Porous media, Conjugate heat transfer, LES,
Double-averaged energy equation, Turbulent heat flux, Dispersion heat flux

*corresponding author
*Email address:* suga@me.osakafu-u.ac.jp (Kazuhiko Suga)

## 1. Introduction

Porous media are widely applied to engineering devices because they may lead to high heat and mass transfer performance of the devices. Although analysing detailed heat and mass transfer rates is required to develop such devises it is usually difficult to measure them inside porous media. Hence, numerical analyses by the volume averaging theory (VAT) of Whitaker (1986, 1996) are usually attempted by engineering researchers. Since flows inside porous media are known to be turbulent at the pore Reynolds number of a few hundred (Jolls and Hanratty, 1966; Dybbs and Edwards, 1984), computation applying the Reynolds averaging coupled with the VAT is common for porous medium turbulence. However, many unknown terms appear in the double-averaged governing equations. They are the volume-averaged Reynolds stress, the dispersive covariance (or dispersion stress) and the drag force term for the momentum equation, and the volume-averaged turbulent heat flux, the dispersion heat flux (or thermal-dispersion), the tortuosity and the wall heat transfer terms for the energy equation. Accordingly, modelling those terms is necessary to close the equation (see Whitaker, 1996; de Lemos, 2006).

In the literature, although almost all models for the double-averaged turbulent flows have been based on the eddy viscosity model (e.g., Nakayama and Kuwahara, 1999, 2008; Pedras and de Lemos, 2001; Foudhill et al., 2005), Ayotte et al. (1999) applied the second-moment closure of Launder et al. (1975) to vegetated flows. The study of Souliotis and Prinos (2011) showed that this second moment closure was better than the $k-\varepsilon$ two-equation eddy

viscosity models of Pedras and de Lemos (2001) and Foudhill et al. (2005) for vegetated flows. The present authors (Kuwata and Suga, 2013a) extended the more advanced two-component-limit second moment closure of Craft and Launder (1996) for porous medium flows adding an extra transport equation of the micro-scale turbulent kinetic energy. Kuwata and Suga (2015c) later refined this model referring to the detailed data of the resolved large eddy simulations of Kuwata and Suga (2013b, 2015a). They showed the superiority of their approach by comparing the model of Ayotte et al. (1999) and popular $k-\varepsilon$ models (Pedras and de Lemos, 2001; Nakayama and Kuwahara, 2008) for the double-averaged system.

For the thermal field, models in porous media are categorized into the local equilibrium and non-equilibrium models. Since the local thermal equilibrium model assumes equality between the solid and fluid temperatures and becomes inadequate in many occasions (e.g., Kaviany, 1995; Quintard and Whitaker, 1993, 1995), more common models are the non-equilibrium models which require macroscopic two-energy equations for the solid and fluid phases. In energy equations for the solid and fluid phases, the tortuosity and wall heat transfer (or interfacial heat transfer) terms appear as interfacial transport terms. Many studies (e.g., Amiri and Vafai, 1994; Hsu et al., 1995; Kuwahara et al., 2001; Nakayama et al., 2001; Yang and Nakayama, 2010) discussed on modelling the tortuosity and wall heat transfer terms.

As for turbulent thermal fields, Saito and de Lemos (2006, 2010) applied the eddy viscosity (diffusivity) model (EVM) and the tensorial gradient diffusion model to the volume-averaged turbulent heat flux (turbulent heat flux plus turbulent thermal dispersion in their notation) and the dispersion heat

flux (thermal dispersion), respectively. For the thermal dispersion, they employed the thermal dispersion tensor of Kuwahara et al. (1996) which was numerically obtained for two-dimensional square rod flows. As Pedras and de Lemos (2008) calculated the thermal dispersion tensor for elliptic rod flows, this tensorial gradient diffusion model requires specific tensor coefficients for each porous medium. A more general approach may be seen in Kuwata and Suga (2015b) who applied the generalized gradient diffusion hypothesis (GGDH) of Daly and Harlow (1970) to the volume-averaged turbulent heat flux for square rod array flows. Although they evaluated the model performance comparing the resolved large eddy simulation (LES) data of Sakurai et al. (2014), the porous structure was limited in the square rod arrays. Accordingly, in this study modelling heat flux terms is discussed for two more different porous media such as staggered cube arrays and body centred cubic foam in addition to the square rod arrays. When porous media are applied to heat exchangers, the actual phenomenon should be conjugate heat transfer with at least spanwise heat flux. Correspondingly, flows with a constant spanwise mean temperature gradient illustrated in Fig.1 are considered.

To provide reference data for turbulent and dispersion heat fluxes, resolved LESs of conjugate heat transfer are performed. Using the LES data, algebraic models of the heat flux terms are discussed through a priori tests. Due to the simplicity of the wall treatment and high computational efficiency with the recent graphical processing unit (GPU) programming, the lattice Boltzmann method (LBM) is very suitable for porous medium flows (e.g., Hatiboglu and Babadagli, 2008; Suga et al., 2009; Suga and Nishio, 2009;

Beugre et al., 2010; Parmigiani et al., 2011; Chukwudozie and Tyagi, 2013; Li et al., 2013; Huang et al., 2015). Since the strategies to perform LES by the LBM have been well established (e.g., Suga et al., 2015; Kuwata and Suga, 2015a), the present study applies the LBM coupled with the wall-adapting local eddy-viscosity (WALE) sub-grid-scale (SGS) model of Nicoud and Ducros (1999). In the LBM, the double-distribution function method which solves the distribution functions for the velocity and the energy density is used. For the velocity and thermal fields, the D3Q27 multiple relaxation time method of Suga et al. (2015) and the regularized D3Q19 single relaxation time method are applied, respectively.

**Nomenclature**

$c_p$ : specific heat

$\mathscr{E}$ : dissipation rate of $\mathcal{K}$

$\mathbf{f}, f_\alpha$ : particle distribution function

$g_\alpha$ : internal energy distribution function

$H_i$ : volume-averaged turbulent heat flux: $\langle \overline{u_i' T'} \rangle^f$

$\mathscr{H}_i$ : dispersion heat flux (thermal-dispersion): $\langle \bar{\tilde{u}}_i \bar{\tilde{T}} \rangle^f$

$k$ : turbulent kinetic energy

$\mathcal{K}$ : dispersive kinetic energy

$T$ : temperature

$T_f$ : fluid temperature

$T_s$ : solid temperature

$U_b$ : bulk velocity

$u_i$ : velocity

$\langle \overline{u_i' u_j'} \rangle^f$ : volume-averaged Reynolds stress

$\langle \tilde{\bar{u}}_i \tilde{\bar{u}}_j \rangle^f$ : dispersive covariance (dispersion stress)

$\varepsilon$ : dissipation rate of $k$

$\varphi$ : porosity

$\Gamma$ : thermal diffusivity

$\Delta^+$ : normalized lattice spacing

$\Delta T$ : imposed temperature difference

$\nu$ : kinematic viscosity

$\rho$ : density

$\overline{\phi}$ : Reynolds-averaged value of $\phi$

$\phi'$ : fluctuation of $\phi$ : $\phi - \overline{\phi}$

$[\phi]$ : plane-averaged value of $\phi$

$\langle \phi \rangle$ : superficial-averaged value of $\phi$

$\langle \phi \rangle^f$ : intrinsic (fluid phase)-averaged value of $\phi$

$\tilde{\phi}$ : dispersion of $\phi$ : $\phi - \langle\phi\rangle^f$

**Acronyms**

BCC : body centred cubic

D3Q19 : three-dimensional 19 discrete velocity

D3Q27 : three-dimensional 27 discrete velocity

EVM : eddy viscosity model

GGDH : generalized gradient diffusion hypothesis

HOGGDH : higher order generalized gradient diffusion hypothesis

LBM : lattice Boltzmann method

LES : large eddy simulation

MRT : multiple-relaxation time

REV : representative elementary volume

SCA : staggered cube arrays

SRA : square rod arrays

SRT : single-relaxation time

VAT : volume averaging theory

WALE : wall-adapting local eddy-viscosity

WET : wealth $\propto$ earnings $\times$ time

## 2. Numerical Scheme of LES

### *2.1. Flow fields*

In this study, the D3Q27 multiple-relaxation time LBM (MRT-LBM) (Suga et al., 2015) is applied to the flow fields. The lattice Boltzmann equation is

$$\begin{aligned} &| \mathbf{f}(\mathbf{x} + \boldsymbol{\xi}_\alpha \delta t, t + \delta t)\rangle - | \mathbf{f}(\mathbf{x}, t)\rangle = \\ &-\mathbf{M}^{-1}\hat{\mathbf{S}} \left\{ | \mathbf{m}(\mathbf{x}, t)\rangle - | \mathbf{m}^{eq}(\mathbf{x}, t)\rangle \right\} - | \mathbf{F}(\mathbf{x}, t)\rangle, \end{aligned} \tag{1}$$

where $\delta t$ is the time step, $\mathbf{f}$ is the particle distribution function and notations such as $|\mathbf{f}\rangle$ is $|\mathbf{f}\rangle = (f_0, f_1, \cdots, f_{26})^T$. See Table 1 for the components of the discrete velocity $\boldsymbol{\xi}_\alpha$ and other parameters. The term $\mathbf{F}$ denotes the external force. The matrix $\mathbf{M}$ is a $27 \times 27$ matrix which linearly transforms $\mathbf{f}$ to the moments $|\mathbf{m}\rangle = \boldsymbol{M}|\mathbf{f}\rangle$. The equilibrium moment $\mathbf{m}^{eq}$ is obtained as $|\mathbf{m}^{eq}\rangle = \mathbf{M}|\mathbf{f}^{eq}\rangle$ with

$$f_\alpha^{eq} = w_\alpha \left( \rho + \rho_0 \left[ \frac{\boldsymbol{\xi}_\alpha \cdot \mathbf{u}}{c_s^2} + \frac{(\boldsymbol{\xi}_\alpha \cdot \mathbf{u})^2 - c_s^2 |\mathbf{u}|^2}{2c_s^4} \right] \right), \tag{2}$$

where $\mathbf{u}$ is the fluid velocity and density $\rho$ is expressed as the sum of constant and fluctuation values: $\rho = \rho_0 + \delta\rho$ (He and Luo, 1997). The sound speed $c_s$ is $c/\sqrt{3}$ where $c = \Delta/\delta t$ with the lattice spacing $\Delta$. See Suga et al. (2015) for the details of the equilibrium moments $\mathbf{m}^{eq}$ and the transformation matrix.

The collision matrix $\hat{\mathbf{S}}$ is diagonal:

$$\begin{aligned} \hat{\mathbf{S}} \equiv diag(&0, 0, 0, 0, s_4, s_5, s_5, s_7, s_7, s_7, s_{10}, \\ &s_{10}, s_{10}, s_{13}, s_{13}, s_{13}, s_{16}, s_{17}, s_{18}, s_{18}, s_{20}, \\ &s_{20}, s_{20}, s_{23}, s_{23}, s_{23}, s_{26}). \end{aligned} \tag{3}$$

Following Suga et al. (2015), the relaxation parameters applied are

$$
\begin{aligned}
&s_4 = 1, 15, s_7 = s_5, s_{10} = 1.5, s_{13} = 1.83, \\
&s_{16} = 1.4, s_{17} = 1.61, s_{18} = s_{20} = 1.98, \\
&s_{23} = s_{26} = 1.74.
\end{aligned} \tag{4}
$$

The macroscopic variables such as $\rho$, the momentum $\rho\mathbf{u}$ and the pressure $p$ are $\rho = \sum_\alpha f_\alpha$, $\rho\mathbf{u} = \sum_\alpha \boldsymbol{\xi}_\alpha f_\alpha$ and $p = c_s^2\rho$, respectively.

The presently applied SGS model is the WALE model (Nicoud and Ducros, 1999):

$$
\begin{aligned}
\nu_{SGS} &= C_w\Delta^2 \frac{\left(S_{ij}^d S_{ij}^d\right)^{3/2}}{\left(S_{ij}S_{ij}\right)^{5/2} + \left(S_{ij}^d S_{ij}^d\right)^{5/4}}, \\
S_{ij} &= \frac{1}{2}\left(\frac{\partial\langle u_i\rangle}{\partial x_j} + \frac{\partial\langle u_j\rangle}{\partial x_i}\right), \\
S_{ij}^d &= \frac{1}{2}\left\{g_{ij}^2 + g_{ji}^2\right\} - \frac{\delta_{ij}}{3}g_{kk}^2, g_{ij} = \frac{\partial\langle u_i\rangle}{\partial x_j},
\end{aligned} \tag{5}
$$

where $\langle u_i\rangle$ is the filtered (or volume-averaged) velocity, and $g_{ij}^2 = g_{ik}g_{kj}$. In the present study, the SGS eddy viscosity coefficient applied is $C_w = 0.1$ (Fröhlich et al., 2005). The sum of the kinematic viscosity $\nu$ and the SGS eddy viscosity $\nu_{SGS}$ is related with the relaxation parameter $s_5$, which is the components of the collision matrix $\hat{\mathbf{S}}$, as

$$
\nu + \nu_{SGS} = c_s^2\left(\frac{1}{s_5} - \frac{1}{2}\right)\delta t. \tag{6}
$$

To consider the effect of $k_{SGS}$, it is added in the external force term in Eq.(1) as

$$
F_\alpha = \frac{\rho w_\alpha \delta t}{c_s^2}\boldsymbol{\xi}_\alpha \cdot \left(-\frac{2}{3}\nabla k_{SGS}\right). \tag{7}
$$

The SGS turbulent energy is estimated by the Simpson method (Inagaki et al., 2010) as

$$k_{SGS} = C_{kes} \sum_{i=1}^{3} \left( \langle u_i \rangle - \langle \langle u_i \rangle \rangle \right)^2 , \tag{8}$$

where $\langle \langle u_i \rangle \rangle$ is the double filtered velocity and the model constant is $C_{kes} = 1$. The estimation procedure for $\langle \langle u_i \rangle \rangle$ is expressed as

$$\langle \langle u_i \rangle \rangle = \frac{1}{2} \langle u_i \rangle + \frac{\langle u_i^E \rangle + \langle u_i^W \rangle + \langle u_i^N \rangle + \langle u_i^S \rangle + \langle u_i^T \rangle + \langle u_i^B \rangle}{12}, \tag{9}$$

where $\langle u_i^E \rangle, \langle u_i^W \rangle, \cdots$ are the velocity components of the neighbouring nodes of node $i$. (It is recognizable that the extra computational cost for $k_{SGS}$ is marginal.)

### *2.2. Thermal fields*

For the thermal fields, the regularized D3Q19 single-relaxation time LBM (SRT-LBM) is applied. (For the D3Q19 SRT-LBM, see a review paper (e.g., Suga, 2013).) The SRT lattice Boltzmann equation is

$$g_\alpha(\mathbf{x} + \boldsymbol{\xi}_\alpha \delta t, t + \delta t) - g_\alpha(\mathbf{x}, t) = -\frac{1}{\tau_g} \left( g_\alpha(\mathbf{x}, t) - g_\alpha^{eq}(\mathbf{x}, t) \right), \tag{10}$$

where $g_\alpha$ is the internal energy distribution function and $\tau_g$ is the relaxation time. Temperature $T$ and the equilibrium part of the distribution function $g_\alpha^{eq}$ are

$$T = \sum_\alpha g_\alpha, \tag{11}$$

and

$$g_\alpha^{eq} = w_\alpha T \left[ 1 + 3 \boldsymbol{\xi}_\alpha \cdot \mathbf{u} \right], \tag{12}$$

respectively.

To stabilize the calculation, the regularization process (Latt and Chopard, 2006) is introduced as

$$g_\alpha(\mathbf{x}+\boldsymbol{\xi}_\alpha\delta t, t+\delta t) = g_\alpha^{eq}(\mathbf{x},t) + \left(1-\frac{1}{\tau_g}\right)\hat{g'}_\alpha(\mathbf{x},t), \tag{13}$$

where $\hat{g'}_\alpha$ is the regularized non-equilibrium part of the distribution function $g'_\alpha$:

$$\hat{g'}_\alpha = w_\alpha \sum_{n=0}^{N} \left\{ \frac{1}{n!} C^{(n)} \mathbf{H}^{(n)}\left(\boldsymbol{\xi}_\alpha/c_s\right) \right\}. \tag{14}$$

For the D3Q19 model, the Hermite expansion coefficients $C^{(n)}$ and the Hermite polynomial $\mathbf{H}^{(n)}$ are

$$C^{(n)} = \sum_\alpha g'_\alpha \mathbf{H}^{(n)}\left(\boldsymbol{\xi}_\alpha/c_s\right), \tag{15}$$

$$\mathbf{H}^{(0)}\left(\boldsymbol{\xi}_\alpha/c_s\right) = 1, \tag{16}$$

$$\mathbf{H}_i^{(1)}\left(\boldsymbol{\xi}_\alpha/c_s\right) = \frac{1}{c_s}\xi_{\alpha i}, \tag{17}$$

$$\mathbf{H}_{ij}^{(2)}\left(\boldsymbol{\xi}_\alpha/c_s\right) = \frac{\xi_{\alpha i}\xi_{\alpha j}}{c_s^2} - \delta_{ij}. \tag{18}$$

From the energy conservation, $C^{(0)} = \sum_\alpha g'_\alpha = 0$ and thus

$$\hat{g'}_\alpha = \frac{w_\alpha}{c_s^2}\xi_{\alpha i}\sum_\beta g'_\beta \xi_{\beta i} + \frac{1}{2}\frac{w_\alpha}{c_s^4}\left(\xi_{\alpha i}\xi_{\alpha j} - c_s^2\delta_{ij}\right)\sum_\beta g'_\beta\left(\xi_{\beta i}\xi_{\beta j} - c_s^2\delta_{ij}\right). \tag{19}$$

The total thermal diffusivity is related to the relaxation time $\tau_g$ as

$$\Gamma = \Gamma_f + \Gamma_{SGS} = c_s^2\left(\tau_g - \frac{1}{2}\right)\delta t, \tag{20}$$

where $\Gamma_f$ is the thermal diffusivity of the fluid and

$$\Gamma_{SGS} = \nu_{SGS}/\mathrm{Pr}_{SGS}, \tag{21}$$

with a constant value of the SGS turbulent Prandtl number of $\mathrm{Pr}_{SGS} = 0.7$.

*2.3. Boundary conditions*

At the wall boundaries, the usual half-way bounce-back method is used for the non-slip velocity condition. With the half-way bounce back method, since the fluid-solid interface is located at the middle of fluid and solid node points, any special treatment is not needed for the conjugate heat transfer (Wang et al., 2007). Thus, between the interfaces

$$g^{fluid}(\mathbf{x}+\boldsymbol{\xi}_\alpha\delta t, t+\delta t) = g^{solid}(\mathbf{x}, t), \tag{22}$$

$$g^{solid}(\mathbf{x}+\boldsymbol{\xi}_\alpha\delta t, t+\delta t) = g^{fluid}(\mathbf{x}, t), \tag{23}$$

can be applied.

For adiabatic thermal boundaries, since the internal energy distribution function may be written as

$$g_\alpha = g_\gamma, \tag{24}$$

where $\alpha$ and $\gamma$ satisfy the relation $\boldsymbol{\xi}_\gamma = \boldsymbol{\xi}_\alpha - 2(\boldsymbol{\xi}_\alpha \cdot \mathbf{n})\mathbf{n}$.

For the isothermal boundary condition, following Yoshino and Inamuro (2003),

$$g_\alpha = w_\alpha \left( \frac{T_{BC} - \sum_{k(\boldsymbol{\xi_k}\cdot\mathbf{n}\leq 0)} g_k}{\sum_{k(\boldsymbol{\xi_k}\cdot\mathbf{n}>0)} w_k} \right), \tag{25}$$

is applied with a prescribed boundary temperature $T_{BC}$.

## 3. Results and discussions

Fig.2 illustrates the presently considered porous media. They are square rod arrays (SRA), staggered cube arrays (SCA) and body centred cubic (BCC) foam as in Kuwata and Suga (2015a). Computational domains, coordinate systems and the representative elementary volumes (REVs) which

are used for the discussion of the volume averaging are also shown. Table 2 lists the Reynolds number, domain size, grid node numbers, porosity $\varphi$ and normalized grid spacing $\Delta^+$ in the present computations. The Reynolds number applied in this study is $Re = hU_b/\nu$ in cases SRA and SCA whilst $Re = DU_b/\nu$ for case BCC, where $h$ is the spacing between obstacles, $D$ is the pore diameter and $U_b = \langle \bar{u} \rangle^f$ is the bulk velocity which corresponds to the streamwise fluid phase double-averaged velocity. The Reynolds numbers considered are Re=1000 and 3000 for cases SRA and SCA while Re=475 and 700 for case BCC. The larger Reynolds numbers are set to be comparable to those of Kuwata and Suga (2015a) though slightly smaller Re (=700) is chosen for case BCC because of the limitation of the computer resources. The grid resolutions and domain sizes were previously confirmed to be satisfactory by grid sensitivity tests in Suga and Kuwata (2014); Kuwata and Suga (2015a). Porosities of $\varphi \geq 0.5$ are considered, and thus $\varphi = 0.52 - 0.90$, $\varphi = 0.48 - 0.71$ and $\varphi = 0.76 - 0.91$ are discussed for cases SRA, SCA and BCC, respectively. For case SCA, higher porosity cases are not considered since the interconnected structure cannot be maintained at $\varphi > 0.75$, while for case BCC lower porosity cases are not considered because all pores become isolated at $\varphi < 0.68$. As shown in Table 2, the lattice (grid) spacing $\Delta^+$ based on the averaged friction velocity ranges from 1.6 to 10.6 depending on the Reynolds number and the porosity of each case. The grid resolutions are in the similar range to those used in Kuwata and Suga (2015a). Note that the wall adjacent node points are situated at $\Delta/2$ from the walls.

Between the upper ($z/H = 2$) and the lower ($z/H = 0$) faces, a constant temperature difference condition is imposed for the solid phase while the

adiabatic condition is applied to the fluid phase. For the flow fields, a slip boundary condition is applied to the upper and lower faces. With these boundary conditions, a fully developed flow with a constant spanwise mean temperature gradient can be achieved inside the REV if its region is defined properly. Indeed, such flow and thermal conditions are confirmed later with Figs.4 and 5.

Periodic boundary conditions are applied to the other faces of the flow and thermal fields. On the solid wall surfaces, the half-way bounce-back boundary condition of the velocity fields is applied for non slip walls. For the conjugate heat transfer at the wall surfaces, any special thermal boundary treatment is unnecessary as aforementioned. The fluid is driven by a constant pressure difference in the streamwise ($x$) direction. The fluid Prandtl number is set to $Pr = 0.71$. The ratio of the thermal diffusivity between the solid and fluid phases is $\Gamma_s/\Gamma_f = 4.4$ which corresponds to the ratio of aluminium and air.

### *3.1. Statistical field quantities*

To provide a general idea of the simulated thermal fields, Fig.3 shows examples of instantaneous temperature fields. The temperatures are normalized by the temperature difference $\Delta T$ between the upper and lower face temperatures. It is seen that the unsteady seamless temperature distributions are produced between the solid-fluid interfaces. This confirms that the present conjugate heat transfer simulations are reasonably performed. For the statistical fields, simulations are continued for 30 turnover times. Fig.4 shows the plane-averaged mean temperature ($[\bar{T}]^s, [\bar{T}]^f$) distributions of the solid and fluid phases in the spanwise ($z$) direction. Superscripts $s$ and $f$

denote solid and fluid phase values, respectively. Due to the slip boundary condition the velocity near the boundaries of $z/H$ =0.0 and 2.0 has non-monotonic profiles leading to slightly non-monotonic temperature distributions near the boundaries. Accordingly, the fluid phase temperature profiles of Fig.4 may not look flat in the vicinity of the boundaries. However, it is confirmed that the temperature gradients vanish at the boundaries corresponding to the adiabatic thermal boundary condition. For cases SRA, SCA and BCC, the plane-averaged mean temperature distributions of $\varphi = 0.90$ at Re=3000, $\varphi = 0.71$ at Re=3000 and $\varphi = 0.91$ at Re=700 are shown, respectively. It is seen that almost linear temperature distributions exist in the region of $0.5 \leq z/H \leq 1.5$. [1] For the corresponding flow fields, Fig.5 shows the plane-averaged Reynolds normal stress distributions. Although boundary effects are seen near the spanwise boundary at $z/H = 0.0$ and 2.0, all the stress components distribute periodically and the boundary effects can be ignored in the region of $0.5 \leq z/H \leq 1.5$. Accordingly, fully developed flows in homogeneous porous media with constant spanwise mean temperature gradients can be assumed when the range is set to $0.5 \leq z/H \leq 1.5$ for the REVs. Notice that because of the periodic thermal boundary condition, mean temperatures are constant in the streamwise ($x$) and $y$ directions.

[1] Since the thermal diffusivity ratio between the solid and fluid phases is quite high, the temperature fluctuation inside the solid-phase is much smaller than that of the fluid-phase. This suggests that almost the same thermal fields may be obtained with a constant spanwise-temperature-gradient condition for the solid-phase.

*3.2. Double-averaged energy equation*

The double averaging (Whitaker, 1986, 1996) consists of the Reynolds and volume averaging. The volume-averaged value $\langle\phi\rangle$ is called the superficial-averaged value while $\langle\phi\rangle^f$ is the fluid phase-averaged value of a variable $\phi$ defined as

$$\langle\phi\rangle = \frac{1}{\Delta V}\int_{\Delta V_f} \phi dv, \tag{26}$$

$$\langle\phi\rangle^f = \frac{1}{\Delta V_f}\int_{\Delta V_f} \phi dv. \tag{27}$$

Between them, the relation $\langle\phi\rangle = \varphi\langle\phi\rangle^f$ exists with the porosity $\varphi$ of the porous medium. The dispersion is defined as $\tilde{\phi} = \phi - \langle\phi\rangle^f$. The Reynolds-averaged and fluctuation values are $\overline{\phi}$ and $\phi'$, respectively. In the double averaging, the order of the volume and the Reynolds averaging operators are interchangeable and the resultant forms are the same (Pedras and de Lemos, 2000).

The double-averaged energy equations for the fluid and solid phases are derived as follows.

For the fluid phase:

$$\frac{\partial\varphi\langle\overline{T_f}\rangle^f}{\partial t}+\varphi\langle\bar{u}_i\rangle^f\frac{\partial\langle\overline{T_f}\rangle^f}{\partial x_i}=\underbrace{\frac{\partial}{\partial x_i}\left(\Gamma_f\frac{\partial\varphi\langle\overline{T_f}\rangle^f}{\partial x_i}\right)}_{\text{viscous diffusion:}\mathcal{D}_f^\nu}$$
$$-\frac{\partial}{\partial x_i}\left(\varphi\underbrace{\langle\overline{u_i'T_f'}\rangle^f}_{\substack{\text{volume-averaged}\\ \text{turbulent heat flux:}H_i}}+\varphi\underbrace{\langle\bar{\tilde{u}}_i\bar{\tilde{T}}_f\rangle^f}_{\text{dispersion heat flux:}\mathscr{H}_i}\right)$$
$$+\underbrace{\frac{\partial}{\partial x_i}\left(\frac{1}{\Delta V}\int_A n_i\Gamma_f\overline{T_f}dA\right)}_{\text{tortuosity:}S_{T_f}}+\underbrace{\frac{1}{\Delta V}\int_A n_i\Gamma_f\frac{\partial\overline{T_f}}{\partial x_i}dA}_{\text{wall heat transfer:}S_{W_f}}, \tag{28}$$

and for the solid phase

$$\frac{\partial\left(1-\varphi\right)\langle\overline{T_s}\rangle^s}{\partial t}=\underbrace{\frac{\partial}{\partial x_i}\left(\Gamma_s\frac{\partial\left(1-\varphi\right)\langle\overline{T_s}\rangle^s}{\partial x_i}\right)}_{\text{viscous diffusion:}\mathcal{D}_s^\nu}$$
$$\underbrace{-\frac{\partial}{\partial x_i}\left(\frac{1}{\Delta V}\int_A n_i\Gamma_s\overline{T_s}dA\right)}_{\text{tortuosity:}S_{Ts}}\underbrace{-\frac{1}{\Delta V}\int_A n_i\Gamma_s\frac{\partial\overline{T_s}}{\partial x_i}dA}_{\text{wall heat transfer:}S_{W_s}}, \tag{29}$$

where $n_i$ is the wall normal unit vector and the subscript or the superscript $f$ denotes the fluid phase while $s$ denotes the solid phase. The surface integral terms $S_T$ and $S_W$ work as energy exchange terms at the interface between the fluid and solid phases. The volume-averaged turbulent heat flux $H_i$ and the dispersion heat flux $\mathscr{H}_i$ in Eq.(28) are unknown second moments. Note that $H_i$ is decomposed into two parts as

$$H_i=\langle\overline{u_i'T_f'}\rangle^f=\overline{\langle u_i'\rangle^f\langle T_f'\rangle^f}+\langle\overline{\tilde{u}_i'\tilde{T}_f'}\rangle^f, \tag{30}$$

where $\overline{\langle u_i' \rangle^f \langle T_f' \rangle^f}$ and $\langle \widetilde{u_i'} \widetilde{T_f'} \rangle^f$ are namely macro- and micro-scale turbulent heat fluxes, respectively. Note that they were respectively named turbulent heat flux and turbulent thermal-dispersion in some other studies (e.g., Saito and de Lemos, 2006, 2010). With the same mean temperature distributions in both solid and fluid phases, the wall heat transfer terms $S_W$'s vanish in the present REVs for the fully developed porous medium flows. Although tortuosity terms $S_T$'s themselves also vanish, the terms inside the differentiation:

$$\frac{1}{\Delta V} \int_A n_i \Gamma_f \overline{T_f} dA, \tag{31}$$

$$-\frac{1}{\Delta V} \int_A n_i \Gamma_s \overline{T_s} dA, \tag{32}$$

work as extra heat fluxes and are called "tortuosity heat fluxes" hereafter.

Fig.6 shows the spanwise superficial-averaged turbulent heat flux and the dispersion heat flux versus the porosity $\varphi$ at the higher Re cases. The corresponding values of the tortuosity heat flux in the fluid phase are also plotted. They are normalized by the macroscopic heat flux in the spanwise direction of the REV:

$$q_{REV} = -\frac{\lambda}{H} \left( \langle \bar{T}_f \rangle^f_{z=1.5H} - \langle \bar{T}_f \rangle^f_{z=0.5H} \right), \tag{33}$$

where $\lambda$ is the thermal conductivity of the fluid. Accordingly, the normalized superficial-averaged values are defined as

$$H_z^* = \varphi \frac{\rho_f c_{pf} H_z}{q_{REV}}, \tag{34}$$

$$\mathscr{H}_z^* = \varphi \frac{\rho_f c_{pf} \mathscr{H}_z}{q_{REV}}, \tag{35}$$

$$S_{Tz}^* = -\frac{\rho_f c_{pf}}{q_{REV} \Delta V} \int_A n_z \Gamma_f \overline{T_f} dA, \tag{36}$$

where $\rho_f$ and $c_{pf}$ are the fluid density and specific heat, respectively. Note that the streamwise ($x$) and the lateral ($y$) components of the heat fluxes do not exist in the present REVs. As seen in Fig.6, the tortuosity heat flux in case BCC has the opposite sign to those in cases SRA and SCA due to the difference in the porous structures. (BCC consists of pores (void elements) but SRA and SCA consist of rods and cubes (solid elements), respectively.) In any case, the tortuosity heat flux is always smaller than the dispersive heat flux by two to three orders of magnitude and thus its influence is marginal in this study.

Although the structure of case SRA does not change in the spanwise direction, the spanwise dispersive velocity $\bar{\bar{u}}_z$ sometimes exists due to the occasional secondary flows as pointed out by Kuwata and Suga (2015a). Hence, as seen in Fig.6(a), $\mathscr{H}_z^*$ is not always zero though the level of $\mathscr{H}_z^*$ is significantly low compared with that of $H_z^*$. In Fig.6(b), for case SCA $H_z^*$ and $\mathscr{H}_z^*$ are comparable at low porosities. Although $H_z^*$ increases and becomes dominant, $\mathscr{H}_z^*$ does not change very much as the porosity increases. In Fig.6(c), it is seen that $\mathscr{H}_z^*$ of case BCC always maintains a considerable level compared with $H_z^*$ in the simulated range of $\varphi$. It is thus confirmed that the level of the dispersion heat flux significantly changes depending on the porous structure.

As seen Fig.6(a), in case SRA $H_z^*$ increases as the increase of the porosity up to $\varphi \simeq 0.7$ and then decreases. Corresponding to the porosities, the trends of cases SCA and BCC are generally consistent with this trend. The general trend of the dispersion heat flux seems to follow the trend of the turbulent heat flux though it is not clear in case SCA. Since any superficial-averaged

fluid variable becomes zero at $\varphi$=0 at which there is no fluid phase, the superficial-averaged turbulent heat flux $H_z^*$ becomes smaller at the smaller porosities. Also it becomes smaller if the porosity becomes too high since the flow obstacles, which enhance turbulence, shrink in the porous structure. This is also confirmed in Fig.7 that shows the distribution of the superficial-averaged turbulent kinetic energy. (As reported in Kuwata and Suga (2015a), there is the second peak in case SRA at $\varphi \simeq 0.82$ that corresponds to a large-scale perturbation regime by the vortex shedding.)

As for the turbulence quantities such as the Reynolds stress, since the detailed profiles were already reported in Kuwata and Suga (2015a), the present study does not repeat the discussion.

### *3.3. Production terms of heat fluxes*

For the discussion on the second moment modelling, it is useful to see the production terms of the volume-averaged turbulent heat flux and the dispersion heat flux. In the fully developed porous medium flows, the production term of $H_i$ may be written as

$$
\begin{aligned}
P_{H_i} = & \underbrace{\overline{\left\langle \tilde{\overline{u}}_i \tilde{u}'_j \right\rangle^f \frac{\partial \left\langle T'_f \right\rangle^f}{\partial x_j}} + \overline{\left\langle \tilde{\overline{T}}_f \tilde{u}'_j \right\rangle^f \frac{\partial \left\langle u'_i \right\rangle^f}{\partial x_j}}}_{-P^t_{i\theta}} \\
& \underbrace{- \left\langle \left( \overline{\tilde{u}'_i \tilde{u}'_j} + \overline{\tilde{u}'_i \left\langle u'_j \right\rangle^f} \right) \frac{\partial \tilde{\overline{T}}_f}{\partial x_j} \right\rangle^f - \left\langle \left( \overline{\tilde{T}'_f \tilde{u}'_j} + \overline{\tilde{T}'_f \left\langle u'_j \right\rangle^f} \right) \frac{\partial \tilde{\overline{u}}_i}{\partial x_j} \right\rangle^f}_{P^d_{i\theta}} \\
& \underbrace{- \left\langle \overline{u'_i u'_j} \right\rangle^f \frac{\partial \left\langle \overline{T}_f \right\rangle^f}{\partial x_j}}_{P^T_{i\theta}} \underbrace{- \left\langle \overline{T'_f u'_j} \right\rangle^f \frac{\partial \left\langle \overline{u}_i \right\rangle^f}{\partial x_j}}_{P^U_{i\theta}} .
\end{aligned}
\tag{37}
$$

For $\mathscr{H}_i$, the production term is derived as

$$\mathscr{P}_{\mathscr{H}_i} = \underbrace{-\overline{\left\langle \tilde{\overline{u}}_i \tilde{u}'_j \right\rangle^f \frac{\partial \left\langle T'_f \right\rangle^f}{\partial x_j}} - \overline{\left\langle \tilde{\overline{T}}_f \tilde{u}'_j \right\rangle^f \frac{\partial \left\langle u'_i \right\rangle^f}{\partial x_j}}}_{P^t_{i\theta}}$$
$$+ \underbrace{\left\langle \left( \overline{\tilde{u}'_i \tilde{u}'_j} + \overline{\tilde{u}'_i \left\langle u'_j \right\rangle^f} \right) \frac{\partial \tilde{\overline{T}}_f}{\partial x_j} \right\rangle^f + \left\langle \left( \overline{\tilde{T}'_f \tilde{u}'_j} + \overline{\tilde{T}'_f \left\langle u'_j \right\rangle^f} \right) \frac{\partial \tilde{\overline{u}}_i}{\partial x_j} \right\rangle^f}_{-P^d_{i\theta}}$$
$$\underbrace{- \left\langle \tilde{\overline{u}}_i \tilde{\overline{u}}_j \right\rangle^f \frac{\partial \left\langle \overline{T}_f \right\rangle^f}{\partial x_j}}_{\mathscr{P}^T_{i\theta}} \underbrace{- \left\langle \tilde{\overline{T}}_f \tilde{\overline{u}}_j \right\rangle^f \frac{\partial \left\langle \overline{u}_i \right\rangle^f}{\partial x_j}}_{\mathscr{P}^U_{i\theta}}. \tag{38}$$

In fully developed flows in porous media, as reported by Kuwata and Suga (2015a) macro-scale Reynolds stress $\overline{\left\langle u'_i \right\rangle^f \left\langle u'_j \right\rangle^f}$ becomes negligible. Correspondingly, its counterpart in the energy equation: $\overline{\left\langle u'_i \right\rangle^f \left\langle T' \right\rangle^f}$, which is the macro-scale turbulent heat flux, becomes negligible. Hence, as shown in Appendix A, $P^t_{i\theta}$ that is a component of the production term of $\overline{\left\langle u'_i \right\rangle^f \left\langle T' \right\rangle^f}$ is considered to vanish in the fully developed porous medium flows. Indeed, in the present simulations, $P^t_{i\theta}$ is always negligibly small. Furthermore, since there is no mean shear in fully developed flows in homogeneous media, $P^U_{i\theta}$ and $\mathscr{P}^U_{i\theta}$ do not exist. In the present flow conditions, the streamwise ($x$) and the lateral ($y$) components of the dispersion and volume-averaged turbulent heat fluxes do not exist. Accordingly, the remaining terms are

$$P_{H_z} = P^d_{3\theta} + P^T_{3\theta}, \tag{39}$$
$$\mathscr{P}_{\mathscr{H}_z} = -P^d_{3\theta} + \mathscr{P}^T_{3\theta}. \tag{40}$$

Fig.8 presents $P^d_{3\theta}$, $P^T_{3\theta}$ and $\mathscr{P}^T_{3\theta}$ distribution profiles. In case SRA, $P^T_{3\theta}$ is dominant in the simulated porosity range. Since $\mathscr{H}_z$ in case SRA tends to

vanish as in Fig.6(a), its production terms $P^d_{3\theta}$ and $\mathscr{P}^T_{3\theta}$ accord this trend as shown in Fig.8(a). In case SCA shown in Fig.8(b), $P^T_{3\theta}$ is always dominant, and $P^d_{3\theta}$ is found to have some influence on the generation of the dispersion heat flux because $|P^d_{3\theta}|$ exceeds $\mathscr{P}^T_{3\theta}$ at $\varphi \geq 0.58$. In case BCC in Fig.8(c), $P^d_{3\theta}$, $P^T_{3\theta}$ and $\mathscr{P}^T_{3\theta}$ are all comparable. Notably the sign of $P^d_{3\theta}$ is positive which is opposite to that of case SCA. The term $P^d_{i\theta}$ is produced by the complex correlation between turbulence and dispersion that is strongly affected by the structure. Thus, due to the similar structural reason to that for the tortuosity heat flux, it is considered that the positive sign appears for $P^d_{3\theta}$ in case BCC. To support this, the sign of $P^d_{3\theta}$ in case SRA at lower porosities is the same (negative) as that for case SCA as seen in Fig.8(a). Since $P^d_{3\theta}$ exchanges energy between spanwise turbulent and dispersion heat fluxes, the observed phenomenon suggests that energy is transferred from the turbulent to dispersion heat fluxes in a solid elements oriented porous structure such as case SCA while the reverse energy flow occurs in a void elements oriented one like case BCC. In any case, from the levels of the profiles, it is confirmed that the effect of each term cannot be negligible in general.

### *3.4. Heat flux modelling*

In the double-averaged energy equation: Eq.(28), what one needs to close the equation is the sum of the heat flux terms: $H_i + \mathscr{H}_i$. Hence, modelling those terms altogether is desirable since $P^d_{i\theta}$ and $P^t_{i\theta}$ are energy exchange terms between $H_i$ and $\mathscr{H}_i$.

From the WET hypothesis (Launder, 1988), the value of a second moment may be proportional to the product of the generation rate of the second

moment and its time-scale. Accordingly,

$$H_i + \mathscr{H}_i \propto \left(P_{H_i} + \mathscr{P}_{\mathscr{H}_i}\right) \times \left(\tau + \mathscr{T}\right), \tag{41}$$

if the joint time-scale is expressed simply as the sum of each time-scale. The time-scales for $H_i$ and $\mathscr{H}_i$ are considered as $\tau = \langle k \rangle^f / \langle \varepsilon \rangle^f$ and $\mathscr{T} = \mathcal{K}/\mathscr{E}$, respectively. Here, $\langle k \rangle^f$, $\langle \varepsilon \rangle^f$, $\mathcal{K}$ and $\mathscr{E}$ are the volume-averaged turbulent kinetic energy, its dissipation rate, dispersive kinetic energy and its dissipation rate, respectively. Therefore, in the fully developed turbulent porous medium flows, the WET model of $H_i + \mathscr{H}_i$ may be written as

$$H_i + \mathscr{H}_i = -c_\theta \left( \langle \overline{u_i' u_j'} \rangle^f \frac{\partial \left\langle \overline{T_f} \right\rangle^f}{\partial x_j} + \langle \bar{\tilde{u}}_i \bar{\tilde{u}}_j \rangle^f \frac{\partial \left\langle \overline{T_f} \right\rangle^f}{\partial x_j} \right) \left( \frac{\langle k \rangle^f}{\langle \varepsilon \rangle^f} + \frac{\mathcal{K}}{\mathscr{E}} \right), \tag{42}$$

where $\langle \overline{u_i' u_j'} \rangle^f$ and $\langle \bar{\tilde{u}}_i \bar{\tilde{u}}_j \rangle^f$ are the volume-averaged Reynolds stress and the dispersion stress, respectively. Fig.9 compares the simulation data and evaluated values of the WET model by a priori manner using the simulation data. The model coefficient of $c_\theta = 0.05$ is applied to all the cases. Although the general trend seems to be captured, it looks difficult to obtain good prediction for all the cases with a single coefficient. Notice that although the above model form is an explicit expression for heat fluxes, in the condition where mean shear exists and thus $P_{i\theta}^U$ and $\mathscr{P}_{i\theta}^U$ are non-negligible, an implicit expression is derived by the WET hypothesis. This implies that the present form may degrade performance further in the region where mean shear exists. Hence, it would be worth discussing on such an implicit algebraic heat flux model in sheared flows.

When the cross correlation between the dispersion and the turbulence

fluctuation is assumed to be weak, the WET model may be rewritten as

$$H_i + \mathscr{H}_i = -c_\theta \frac{\langle k \rangle^f}{\langle \varepsilon \rangle^f} \langle \overline{u_i' u_j'} \rangle^f \frac{\partial \left\langle \overline{T_f} \right\rangle^f}{\partial x_j} - c_\theta' \frac{\mathcal{K}}{\mathcal{E}} \langle \bar{\tilde{u}}_i \bar{\tilde{u}}_j \rangle^f \frac{\partial \left\langle \overline{T_f} \right\rangle^f}{\partial x_j}, \tag{43}$$

with coefficients $c_\theta$ and $c_\theta'$. Consequently, Eq.(43) becomes the sum of the GGDH models for $H_i$ and $\mathscr{H}_i$. Fig.10 compares the simulation data and evaluated values by the GGDH model with $c_\theta = 0.3$ and $c_\theta' = 0.08$. It is seen that the prediction becomes slightly better than that by the WET model. Although the agreement in higher porosity cases becomes better in all cases, it is still difficult to obtain satisfactory prediction for all the cases with a single set of coefficients. In particular, case BCC seems to be difficult to predict. In case BCC, compared with the other cases, $\mathscr{H}_z$ and thus $\mathscr{P}_{3\theta}^T$ are significantly larger and their levels are quite similar to those of $H_z$ and $P_{3\theta}^T$, respectively, as seen in Figs.6(c) and 8(c). This implies that the coefficient $c_\theta'$ for the dispersion part in Eq.(43) needs to be larger for case BCC though it should be relatively small compared with $c_\theta$ to obtain reasonable levels for cases SRA and SCA. This suggests that for improving the prediction performance, further tensorial expressions for the coefficients are required.

Hence, an expanded version of the GGDH model which is the second order GGDH model (Suga and Abe, 2000; Abe and Suga, 2001), is considered. This model expresses the heat fluxes as

$$H_i + \mathscr{H}_i = -c_\theta \frac{\langle k \rangle^f}{\langle \varepsilon \rangle^f} \frac{\langle \overline{u_i' u_l'} \rangle^f \langle \overline{u_l' u_j'} \rangle^f}{\langle k \rangle^f} \frac{\partial \left\langle \overline{T_f} \right\rangle^f}{\partial x_j} - c_\theta' \frac{\mathcal{K}}{\mathcal{E}} \frac{\langle \bar{\tilde{u}}_i \bar{\tilde{u}}_l \rangle^f \langle \bar{\tilde{u}}_l \bar{\tilde{u}}_j \rangle^f}{\mathcal{K}} \frac{\partial \left\langle \overline{T_f} \right\rangle^f}{\partial x_j}. \tag{44}$$

For this higher order GGDH model (HOGGDH), the model coefficients $c_\theta =$

0.5 and $c'_\theta = 0.3$ are applied. From Fig.11, it is confirmed that the general agreement is improved very much, particularly in case BCC. Indeed, although the GGDH model predicts 45% lower for case BCC of $\varphi = 0.76$ at Re=700, which is the worst prediction case, the HOGGDH improves it to 12% underprediction. Overall, it can be confirmed that the general trends of the sum of the dispersion and volume-averaged turbulent heat fluxes can be well captured by the second order HOGGDH in all the test cases. Note that for the WET, GGDH and HOGGDH models, a second moment closure for porous medium flows such as Kuwata and Suga (2015c) is necessary since they require each component of the Reynolds and dispersion stresses.

The standard model for the turbulent heat flux may be the EVM, which is a kind of reduced version of the GGDH model, the form

$$H_i + \mathscr{H}_i = -c_\theta \frac{\langle k \rangle^f}{\langle \varepsilon \rangle^f} \langle k \rangle^f \frac{\partial \left\langle \overline{T_f} \right\rangle^f}{\partial x_i} - c'_\theta \frac{\mathcal{K}}{\mathcal{E}} \mathcal{K} \frac{\partial \left\langle \overline{T_f} \right\rangle^f}{\partial x_i}, \tag{45}$$

is thus finally examined. Fig.12 compares the simulation data and evaluated values of the EVM with $c_\theta = 0.2$ and $c'_\theta = 0.002$. It is confirmed that the general agreement becomes worse than that by the WET model.

Although they are not shown here, the preliminary model computations by the discussed heat flux models coupled with the second-moment closure of Kuwata and Suga (2015c) show the same trends as those of the a priori tests depending on the heat flux models. This supports the present discussions.

## 4. Conclusions

To discuss modelling the volume-averaged turbulent heat flux and the dispersion heat flux inside porous media, resolved LESs of conjugate heat

transfer in square rod arrays, staggered cube arrays and body centred cubic foam are performed by the LBM. Since the production terms of the volume-averaged turbulent heat flux and the dispersion heat flux include mutual energy exchange terms, it is shown that applying the WET hypothesis to the sum of those fluxes leads to a simple model form. By modifying this WET model, the GGDH and HOGGDH models are derived. From a priori tests using the LES data, it is found that the HOGGDH model performs well for all the tested cases. Although the GGDH model slightly improves the results by the WET model, the WET and GGDH models are not always good enough, particularly in the body centred cubic foam. From further tests with the EVM, it is confirmed that the EVM deteriorates the prediction of the WET model.

**Acknowledgements**

The authors thank M. Kaneda, Y. Sakurai and K. Tsuda for their support to this study. The numerical simulations were carried out in the joint research project: jh160042, supported by JHPCN using TSUBAME2.5 supercomputer in Tokyo Institute of Technology, Japan.

## Appendix A

The production term for the macro-scale turbulent heat flux:$\overline{\langle u_i' \rangle^f \langle T_f' \rangle^f}$, may be written as

$$P_{H_i}^M = \underbrace{\overline{\left\langle \tilde{\overline{u}}_i \tilde{u}_j' \right\rangle^f \frac{\partial \left\langle T_f' \right\rangle^f}{\partial x_j}} + \overline{\left\langle \tilde{\overline{T}}_f \tilde{u}_j' \right\rangle^f \frac{\partial \left\langle u_i' \right\rangle^f}{\partial x_j}}}_{-P_{i\theta}^t} - \overline{\langle u_i' \rangle^f \langle u_j' \rangle^f} \frac{\partial \left\langle \overline{T}_f \right\rangle^f}{\partial x_j} - \overline{\langle u_i' \rangle^f \langle T_f' \rangle^f} \frac{\partial \left\langle \overline{u}_i \right\rangle^f}{\partial x_j}, \tag{46}$$

while for the micro-scale turbulent heat flux: $\langle \overline{\tilde{u}_i' \tilde{T}_f'} \rangle^f$,

$$P_{H_i}^m = \underbrace{-\left\langle \left( \overline{\tilde{u}_i' \tilde{u}_j'} + \overline{\tilde{u}_i' \left\langle u_j' \right\rangle^f} \right) \frac{\partial \tilde{\overline{T}}_f}{\partial x_j} \right\rangle^f - \left\langle \left( \overline{\tilde{T}_f' \tilde{u}_j'} + \overline{\tilde{T}_f' \left\langle u_j' \right\rangle^f} \right) \frac{\partial \tilde{\overline{u}}_i}{\partial x_j} \right\rangle^f}_{P_{i\theta}^d} - \langle \overline{\tilde{u}_i' \tilde{u}_j'} \rangle^f \frac{\partial \left\langle \overline{T}_f \right\rangle^f}{\partial x_j} - \langle \overline{\tilde{u}_i' \tilde{T}_f'} \rangle^f \frac{\partial \left\langle \overline{u}_i \right\rangle^f}{\partial x_j}, \tag{47}$$

is derived.

## References


Abe, K., Suga, K., 2001. Toward the development of a Reynolds-averaged algebraic turbulent scalar-flux model. Int. J. Heat Fluid Flow 22, 19–29.

Amiri, A., Vafai, K., 1994. Analysis of dispersion effects and non-thermal equilibrium, non Darcian, variable porosity incompressible flow through porous media. Int. J. Heat Mass Transfer 37, 939–954.

Ayotte, K.W., Finnigan, J.J., Raupach, M.R., 1999. A second-order closure for neutrally stratified vegetative canopy flows. Boundary Layer Meteorol. 90, 189–216.

Beugre, D., Calvo, S., Dethier, G., Crine, M., Toye, D., Marchot, P., 2010. Lattice Boltzmann 3D flow simulations on a metallic foam. J. Comput. Appl. Math. 234, 2128 – 2134.

Chukwudozie, C., Tyagi, M., 2013. Pore scale inertial flow simulations in 3-d smooth and rough sphere packs using lattice Boltzmann method. AIChE J. 59, 4858–4870.

Craft, T.J., Launder, B.E., 1996. A Reynolds stress closure designed for complex geometries. Int. J. Heat Fluid Flow 17, 246–254.

Daly, B.J., Harlow, F.H., 1970. Transport equation in turbulence. Phys. Fluids 13, 2634–2649.

Dybbs, A., Edwards, R.V., 1984. A new look at porous media fluid mechanics-Darcy to turbulent, in: Bear, J., Corapcioglu, M.Y. (Eds.), Fundamentals of Transport Phenomena in Porous Media. Springer Netherlands. volume 82 of *NATO ASI Series*, pp. 199–256.

Foudhill, H., Brunet, Y., Caltagirone, J.P., 2005. A fine-scale $k - \varepsilon$ model for atmospheric flow over heterogeneous landscapes. Environ. Fluid Mech. 5, 247–265.

Fröhlich, J., Mellen, C.P., Rodi, W., Temmerman, L., Leschziner, M.A., 2005. Highly resolved large-eddy simulation of separated flow in a channel with streamwise periodic constrictions. J. Fluid Mech. 526, 19–66.

Hatiboglu, C.U., Babadagli, T., 2008. Pore-scale studies of spontaneous imbibition into oil-saturated porous media. Phys. Rev. E 77, 066311.

He, X., Luo, L.S., 1997. Lattice Boltzmann model for the incompressible Navier-Stokes equation. J. Stat. Phys. 88, 927–944.

Hsu, C.T., Cheng, P., Wong, K.W., 1995. A lumped-parameter model for stagnant thermal conductivity of spatially periodic porous media. J. Heat Transfer 117, 264–269.

Huang, C., Shi, B., He, N., Chai, Z., 2015. Implementation of multi-GPU based lattice Boltzmann method for flow through porous media. Adv. Appl. Math. Mech. , 1–12.

Inagaki, M., Nagaoka, M., Horiuchi, N., Suga, K., 2010. Large eddy simulation analysis of engine steady intake flows using a mixed-time-scale subgrid-scale model. Int. J. Engine Res. 11, 229–241.

Jolls, K.R., Hanratty, T.J., 1966. Transition to turbulence for flow through a dumped bed of spheres. Chem. Eng. Sci. 21, 1185 – 1190.

Kaviany, M., 1995. Principles of heat transfer in porous media. 2nd ed., Springer, New York.

Kuwahara, F., Nakayama, A., Koyama, H., 1996. A numerical study of thermal dispersion in porous media. J. Heat Transfer 118, 756–761.

Kuwahara, F., Shirota, M., Nakayama, A., 2001. A numerical study of interfacial convective heat transfer coefficient in two-energy equation model for convection in porous media. Int. J. Heat Mass Transfer 44, 1153–1159.

Kuwata, Y., Suga, K., 2013a. Modelling turbulence around and inside porous

media based on the second moment closure. Int. J. Heat Fluid Flow 43, 35 – 51.

Kuwata, Y., Suga, K., 2013b. A study on the volume averaged turbulence transport equations by performing LES of square rod array flows. Trans. Japan Soc. Mech. Engrs.(B) 79, 1752–1763. (in Japanese).

Kuwata, Y., Suga, K., 2015a. Large eddy simulations of pore-scale turbulent flows in porous media by the lattice Boltzmann method. Int. J. Heat Fluid Flow 55, 143–157.

Kuwata, Y., Suga, K., 2015b. Porous medium modelling of turbulent heat transfer in square rod arrays with a multi-scale second moment closure. Spec. Top. Rev. Porous Med. 6, 173–184.

Kuwata, Y., Suga, K., 2015c. Progress in the extension of a second-moment closure for turbulent environmental flows. Int. J. Heat Fluid Flow 51, 268–284.

Latt, J., Chopard, B., 2006. Lattice Boltzmann method with regularized pre-collision distribution functions. Math. Comput. Simul. 72, 165–168.

Launder, B., Reece, G., Rodi, W., 1975. Progress in the development of a Reynolds-stress turbulence closure. J. Fluid Mech. 68, 537–566.

Launder, B.E., 1988. On the computation of convective heat transfer in complex turbulent flows. J. Heat Transfer 110, 1112–1129.

de Lemos, M.J.S., 2006. Turbulence in porous media. Elsevier, UK.

Li, X., Zhang, Y., Wang, X., Ge, W., 2013. GPU-based numerical simulation of multi-phase flow in porous media using multiple-relaxation-time lattice Boltzmann method. Chem. Eng. Sci. 102, 209 – 219.

Nakayama, A., Kuwahara, F., 1999. A macroscopic turbulence model for flow in a porous medium. J. Fluids Engrg. 121, 427–433.

Nakayama, A., Kuwahara, F., 2008. A general macroscopic turbulence model for flows in packed beds, channels, pipes, and rod bundles. J. Fluids Engrg. 130, 101205–1–7.

Nakayama, A., Kuwahara, F., Sugiyama, M., Xu, G., 2001. A two-energy equation model for conduction and convection in porous media. Int. J. Heat Mass Transfer 44, 4375 – 4379.

Nicoud, F., Ducros, F., 1999. Subgrid-scale stress modelling based on the square of the velocity gradient tensor. Flow Turbulence Combust. 62, 183–200.

Parmigiani, A., Huber, C., Bachmann, O., Chopard, B., 2011. Pore-scale mass and reactant transport in multiphase porous media flows. J. Fluid Mech. 686, 40–76.

Pedras, M.H.J., de Lemos, M.J.S., 2000. On the definition of turbulent kinetic energy for flow in porous media. Int. Commun. Heat Mass Transfer 27, 211–220.

Pedras, M.H.J., de Lemos, M.J.S., 2001. Macroscopic turbulence modeling for incompressible flow through undeformable porous media. Int. J. Heat Mass Transfer 44, 1081–1093.

Pedras, M.H.J., de Lemos, M.J.S., 2008. Thermal dispersion in porous media as a function of the solid-fluid conductivity ratio. Int. J. Heat Mass Transfer 51, 5359–5367.

Quintard, M., Whitaker, S., 1993. One- and two-equation models for transient diffusion processes in two-phase systems. Adv. Heat Transfer 23, 369–367.

Quintard, M., Whitaker, S., 1995. Local thermal equilibrium for transient heat conduction: theory and comparison with numerical experiments. Int. J. Heat Mass Transfer 38, 2779 – 2796.

Saito, M.B., de Lemos, M.J., 2006. A correlation for interfacial heat transfer coefficient for turbulent flow over an array of square rods. J. Heat Transfer 128, 444–452.

Saito, M.B., de Lemos, M.J.S., 2010. A macroscopic two-energy equation model for turbulent flow and heat transfer in highly porous media. Int. J. Heat Mass Transfer 53, 2424–2433.

Sakurai, Y., Kuwata, Y., Suga, K., 2014. Lattice Boltzmann LES of conjugate turbulent heat transfer in square rod arrays, in: Proc.10th International ERCOFTAC Symposium on Engineering Turbulence Modelling and Measurements, Marbella, Spain.

Souliotis, D., Prinos, P., 2011. Macroscopic turbulence models and their application in turbulent vegetated flows. J. Hydraulic Eng. 137, 315–332.

Suga, K., 2013. Lattice Boltzmann methods for complex micro-flows: applicability and limitations for practical applications. Fluid Dyn. Res. 45, 034501.

Suga, K., Abe, K., 2000. Nonlinear eddy viscosity modelling for turbulence and heat transfer near wall and shear-free boundaries. Int. J. Heat Fluid Flow 21, 37–48.

Suga, K., Kuwata, Y., 2014. On the budget terms of the double averaged turbulent stress transport equations in porous media. Procedia Eng. 79, 3–8.

Suga, K., Kuwata, Y., Takashima, K., Chikasue, R., 2015. A D3Q27 multiple-relaxation-time lattice Boltzmann method for turbulent flows. Comput. Math. Appl. 69, 518–529.

Suga, K., Nishio, Y., 2009. Three dimensional microscopic flow simulation across the interface of a porous wall and clear fluid by the lattice Boltzmann method. The Open Transp. Phenom. J. 1, 35–44.

Suga, K., Tanaka, T., Nishio, Y., Murata, M., 2009. A boundary reconstruction scheme for lattice Boltzmann flow simulation in porous media. Prog. Comput. Fluid Dyn. 9, 201–207.

Wang, J., Wang, M., Li, Z., 2007. A lattice Boltzmann algorithm for fluid-solid conjugate heat transfer. Int. J. Therm. Sci. 46, 228 – 234.

Whitaker, S., 1986. Flow in porous media I: A theoretical derivation of Darcy's law. Transp. Porous Med. 1, 3–25.

Whitaker, S., 1996. The Forchheimer equation: A theoretical development. Transp. Porous Med. 25, 27–61.

Yang, C., Nakayama, A., 2010. A synthesis of tortuosity and dispersion in effective thermal conductivity of porous media. Int. J. Heat Mass Transfer 53, 3222 – 3230.

Yoshino, M., Inamuro, T., 2003. Lattice Boltzmann simulations for flow and heat/mass transfer problems in a three-dimensional porous structure. Int. J. Numer. Meth. Fluids 43, 183–198.

Table 1: Parameters of the discrete velocity models.

| Model | $c_s/c$ | $\boldsymbol{\xi}_\alpha/c$ | $w_\alpha$ |
|---|---|---|---|
| D3Q19 | $1/\sqrt{3}$ | $(0,0,0)$ | $1/3(\alpha=0)$ |
| | | $(\pm1,0,0),(0,\pm1,0),(0,0,\pm1)$ | $1/18(\alpha=1,\cdots,6)$ |
| | | $(\pm1,\pm1,0),(\pm1,0,\pm1),(0,\pm1,\pm1)$ | $1/36(\alpha=7,\cdots,18)$ |
| D3Q27 | $1/\sqrt{3}$ | $(0,0,0)$ | $8/27(\alpha=0)$ |
| | | $(\pm1,0,0),(0,\pm1,0),(0,0,\pm1)$ | $2/27(\alpha=1,\cdots,6)$ |
| | | $(\pm1,\pm1,0),(\pm1,0,\pm1),(0,\pm1,\pm1)$ | $1/54(\alpha=7,\cdots,18)$ |
| | | $(\pm1,\pm1,\pm1)$ | $1/216(\alpha=19,\cdots,26)$ |

Table 2: Computational domains and grid node numbers for LESs.

| case | Re | domain $x\times y\times z$ | Node numbers $x\times y\times z$ | $\varphi$ | $\Delta^+$ |
|---|---|---|---|---|---|
| SRA | 1000 | $4H\times H\times 2H$ | $321\times 81\times 160$ | 0.52–0.9 | 2.9–5.9 |
| | 3000 | $4H\times H\times 2H$ | $321\times 81\times 160$ | 0.52–0.9 | 4.9–10.3 |
| SCA | 1000 | $4H\times 2H\times 2H$ | $320\times 160\times 160$ | 0.48–0.71 | 4.2–5.9 |
| | 3000 | $4H\times 2H\times 2H$ | $320\times 160\times 160$ | 0.48–0.71 | 7.3–10.6 |
| BCC | 475 | $2H\times 2H\times 2H$ | $200\times 200\times 200$ | 0.76–0.91 | 1.6–2.4 |
| | 700 | $2H\times 2H\times 2H$ | $200\times 200\times 200$ | 0.76–0.91 | 2.0–2.9 |

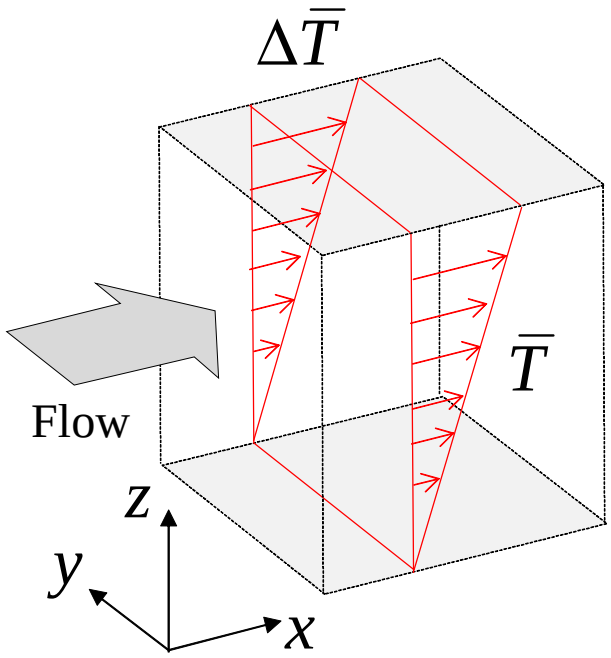


Figure 1: Constant spanwise mean temperature gradient.

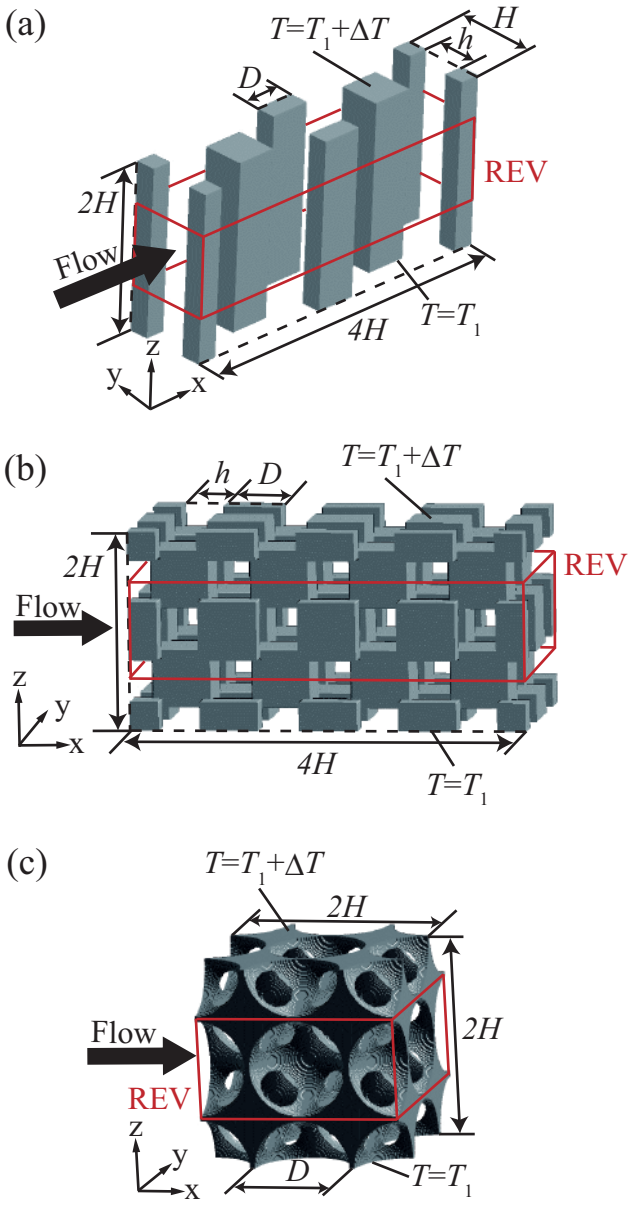


Figure 2: Model geometries and computational domains of porous media: (a) square rod arrays (SRA), (b) staggered cube arrays (SCA), (c) body centred cubic (BCC) foam.

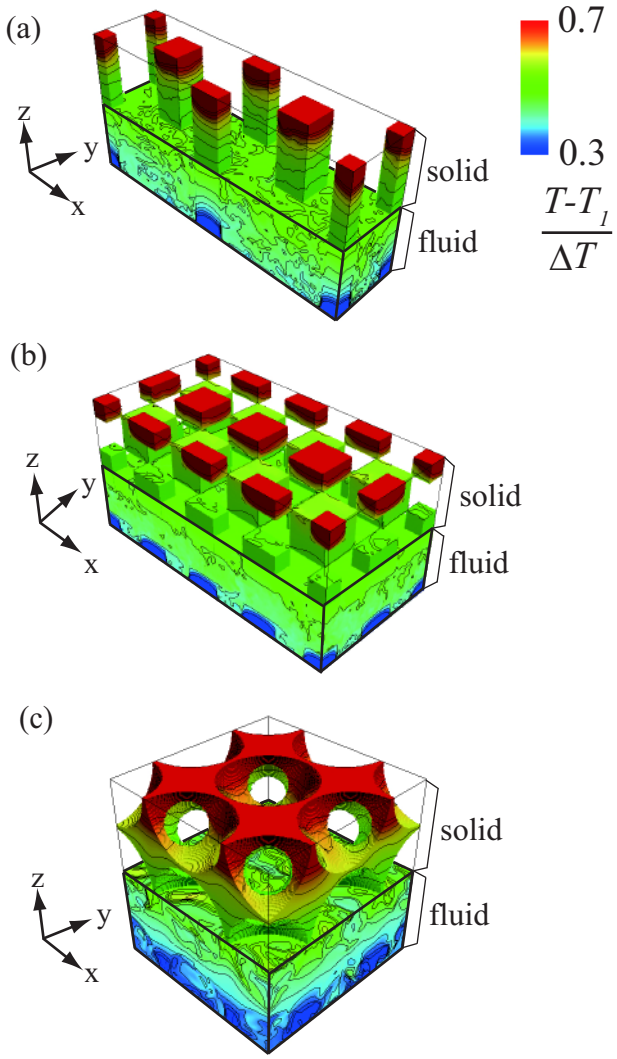


Figure 3: Instantaneous temperature distributions of fluid and solid phases: (a) case SRA of $\varphi = 0.82$ at Re=3000, (b) case SCA of $\varphi = 0.71$ at Re=3000, (c) case BCC of $\varphi = 0.84$ at Re=475.

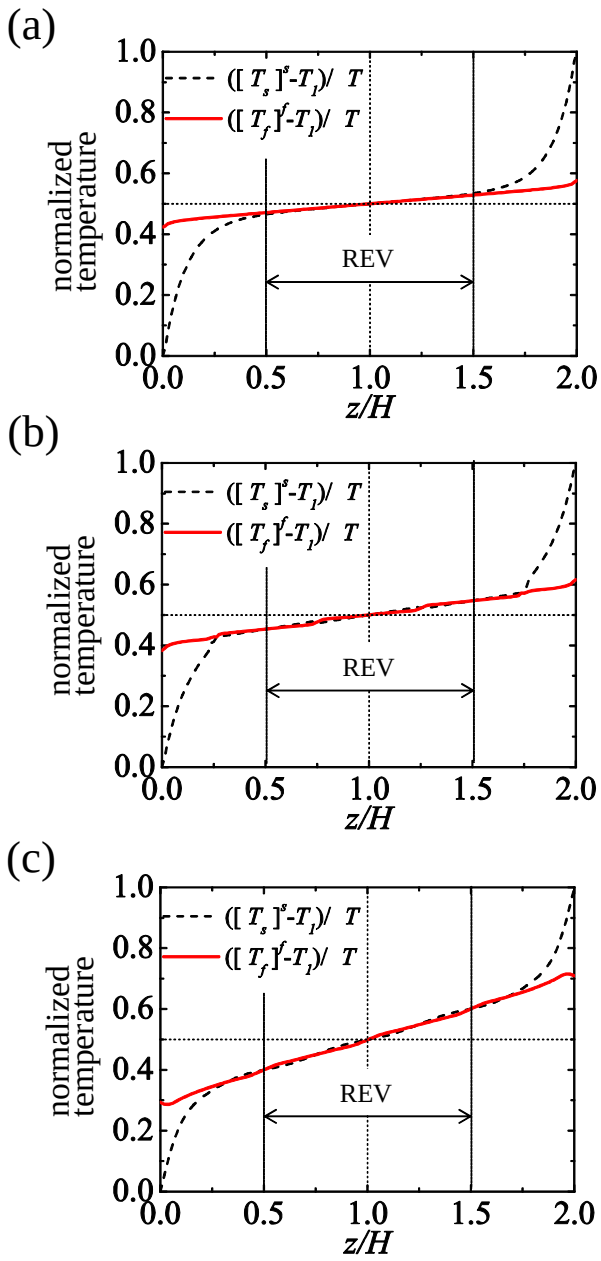


Figure 4: Plane-averaged mean temperature distributions in the spanwise ($z$) direction: (a) case SRA of $\varphi = 0.90$ at Re =3000, (b) case SCA of $\varphi = 0.71$ at Re=3000, (c) case BCC of $\varphi = 0.91$ at Re=700.

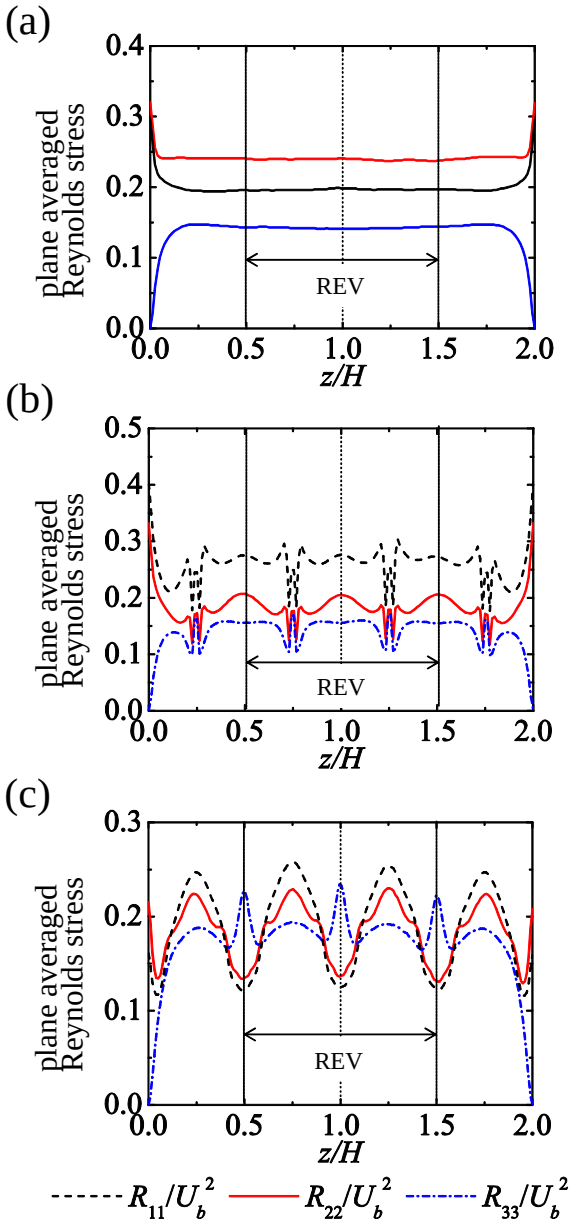


Figure 5: Plane-averaged Reynolds stress distributions in the spanwise ($z$) direction: (a) case SRA of $\varphi = 0.90$ at Re=3000, (b) case SCA of $\varphi = 0.71$ at Re=3000, (c) case BCC of $\varphi = 0.91$ at Re=700; $R_{11} = [\overline{u'u'}]^f$, $R_{22} = [\overline{v'v'}]^f$,$R_{33} = [\overline{w'w'}]^f$.

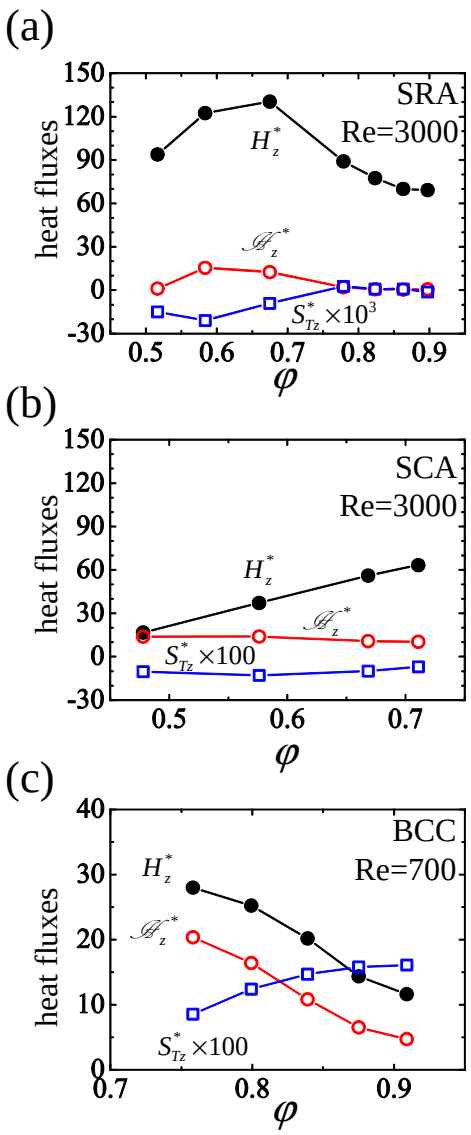


Figure 6: Normalized superficial-averaged spanwise heat fluxes: (a) case SRA at Re=3000 (b) case SCA at Re=3000, (c) case BCC at Re=700; normalized turbulent heat flux: $H_z^* = \varphi\rho_f c_{pf} H_z/q_{REV}$, normalized dispersion heat flux: $\mathscr{H}_z^* = \varphi\rho_f c_{pf}\mathscr{H}_z/q_{REV}$, normalized tortuosity heat flux: $S_{Tz}^* = -\rho_f c_{pf}\int_A n_z \Gamma_f \overline{T_f} dA/(q_{REV}\Delta V)$.

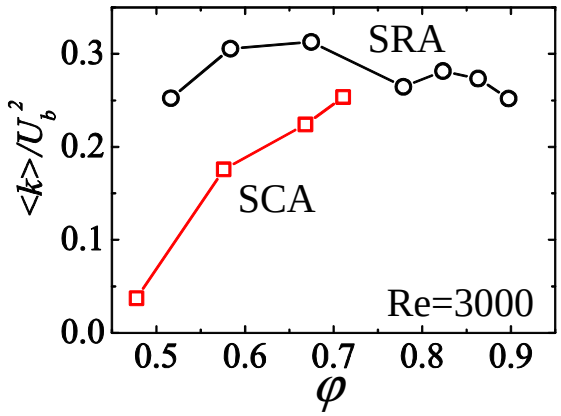


Figure 7: Superficial-averaged turbulent kinetic energy of cases SRA and SCA at Re=3000.

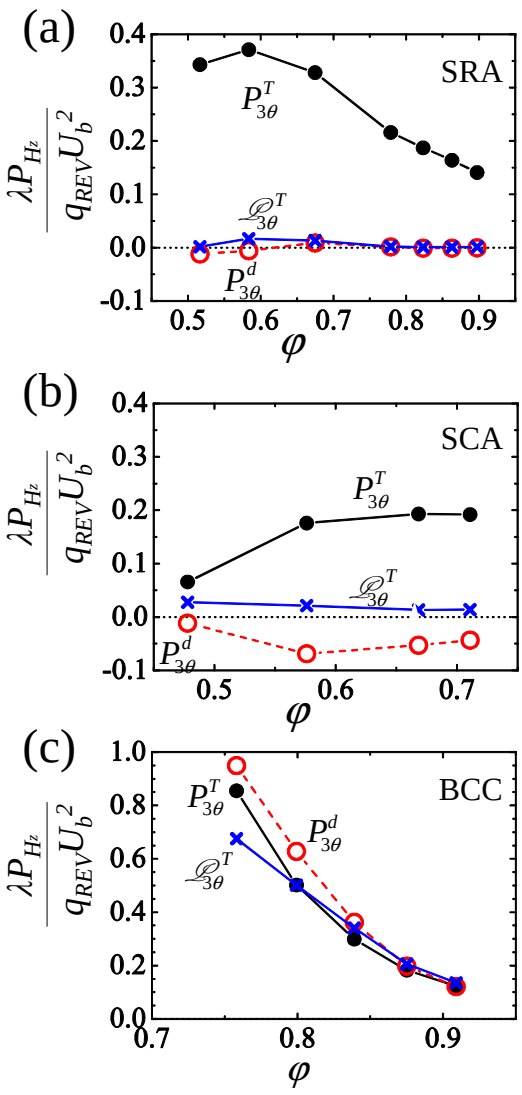


Figure 8: Production terms of the spanwise heat fluxes: (a) case SRA at Re=3000, (b) case SCA at Re=3000, (c) case BCC at Re=700.

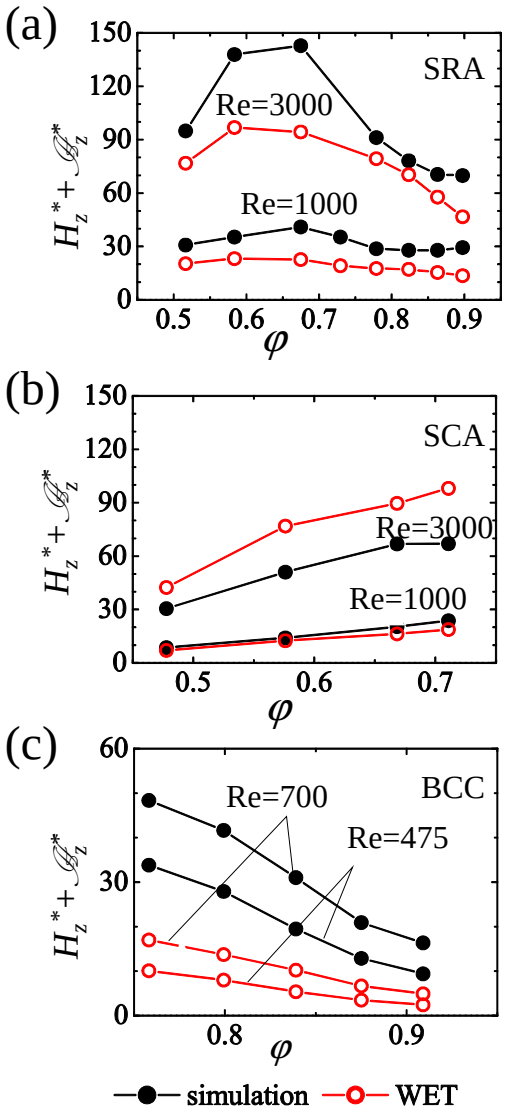


Figure 9: Spanwise heat fluxes and the estimated values by the WET model versus porosity: (a) case SRA, (b) case SCA, (c) case BCC.

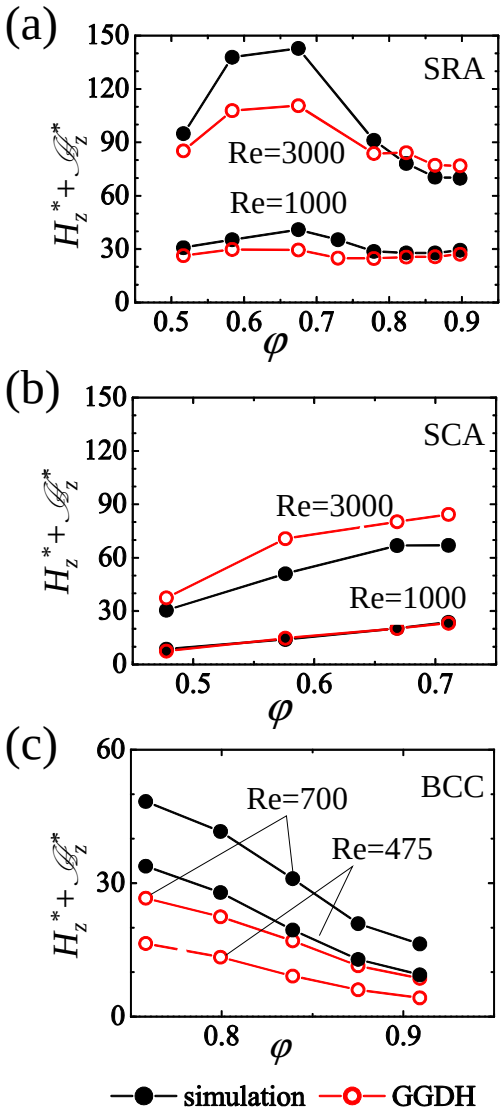


Figure 10: Spanwise heat fluxes and the estimated values by the GGDH model versus porosity: (a) case SRA, (b) case SCA, (c) case BCC.

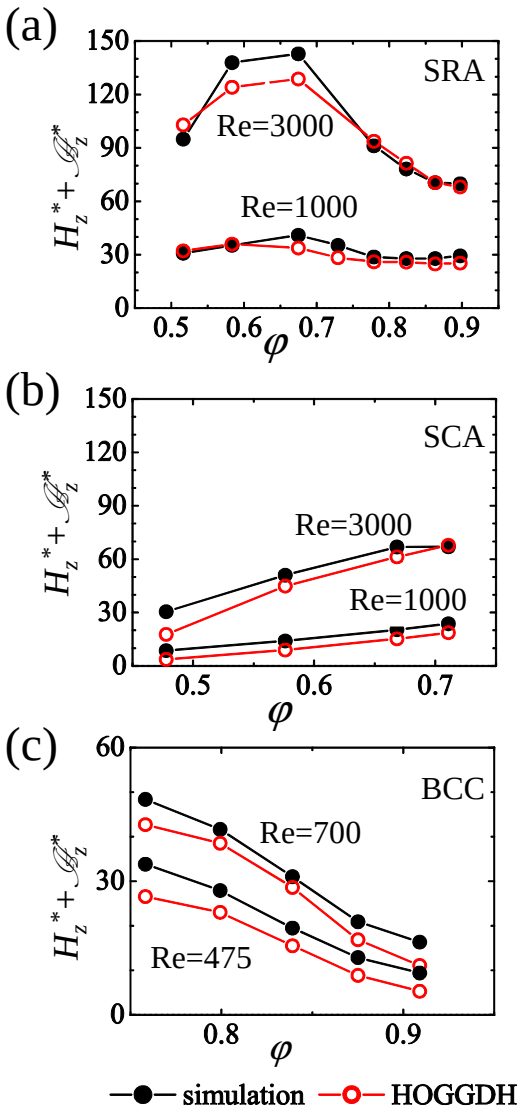


Figure 11: Spanwise heat fluxes and the estimated values by the HOGGDH model versus porosity: (a) case SRA, (b) case SCA, (c) case BCC.

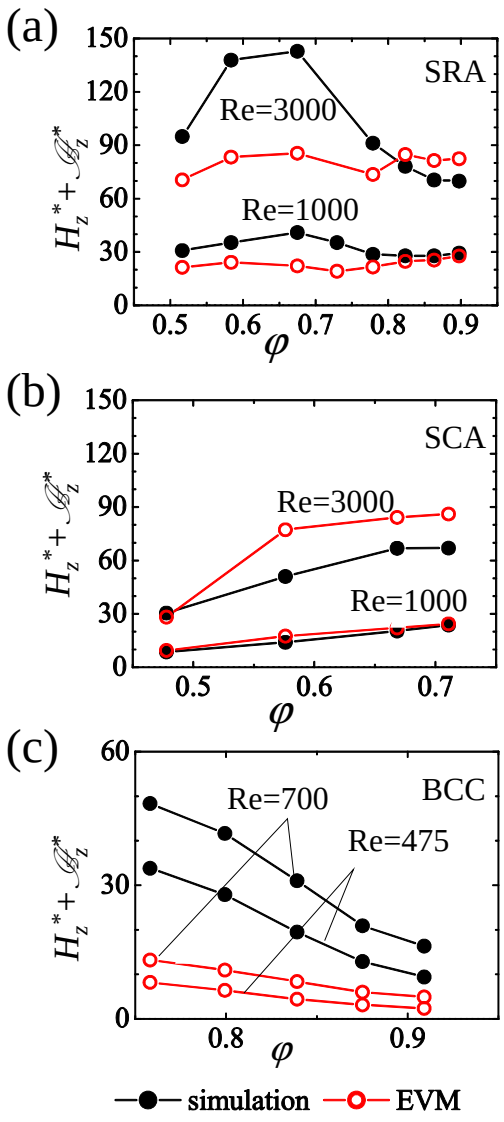


Figure 12: Spanwise heat fluxes and the estimated values by the EVM model versus porosity: (a) case SRA, (b) case SCA, (c) case BCC.